SCIENTIFIC REPORTS
nature research

OPEN

CH_3NH_3Br solution as a novel platform for the selective fluorescence detection of Pb^{2+} ions

Jun Yan[1], Yuchun He[1], Yunlin Chen[1*], Yongzhe Zhang[2*] & Hui Yan[2]

The development of a simple fluorescent sensor for detecting the Pb^{2+} heavy metal is fundamentally important. The $CH_3NH_3PbBr_3$ perovskite material exhibits excellent photoluminescence properties that are related to Pb^{2+}. Based on the effects of Pb^{2+} on the luminescent properties of $CH_3NH_3PbBr_3$, we design a novel platform for the selective fluorescence detection of Pb^{2+} ions. Herein, we use a CH_3NH_3Br solution at a high concentration as the fluorescent probe. Incorporation of $PbBr_2$ into the CH_3NH_3Br solution results in a rapid chemical reaction to form $CH_3NH_3PbBr_3$. Hence, the nonfluorescent CH_3NH_3Br material displays a sensitive and selective luminescent response to Pb^{2+} under UV light illumination. Moreover, the reaction between CH_3NH_3Br and $PbBr_2$ could transform Pb^{2+} into $CH_3NH_3PbBr_3$, and therefore, CH_3NH_3Br may also be used to extract Pb^{2+} from liquid waste in recycling applications.

In the past several decades, the control of heavy metal pollution has been the focal point of environmental protection efforts[1–6]. Development of simple and selective sensors is critical for detection of heavy metals. Several methods such as atomic absorption spectrometry (AAS)[7], inductively coupled plasma-mass spectrometry (ICP-MS)[8], inductively coupled plasma atomic-emission spectroscopy (ICP-AES)[9], electrochemical methods[10], and fluorescent techniques[11] have been devised to detect heavy metals. Compared with other methods, the fluorescence-based methods display many advantages such as low cost, high sensitivity, rapid detection, and ease of use[12]. As fluorescent materials, lead halide perovskite $CH_3NH_3PbBr_3$ ($MAPbBr_3$) and $CsPbBr_3$ show excellent luminescent properties including bright photoluminescence (PL), high PL quantum yields (PLQY), and narrow bandwidth[13–15]. Compared with $MAPbBr_3$, the PL emission peaks of $MAPbI_3$ and $MAPbCl_3$ are red and blue light, respectively, which can't be excited by a UV lamp. Due to these advantages, the $MAPbBr_3$ and $CsPbBr_3$ have been used in light-emitting diodes (LED)[16–22] and fluorescence sensors or detectors[12,23]. Chinnadurai *et al.*[24] reported that fluorescent $MAPbBr_3$ nanoparticles can be used as an excellent sensor for the detection of 2, 4, 6-trinitrophenol (TNP). Liu *et al.*[25] used $CsPbBr_3$ perovskite quantum dots as photoluminescent probe for selective detection of Cu^{2+}. Zhang *et al.*[12] encapsulated $MAPbBr_3$ perovskite quantum dots in MOF-5 matrix as a stable fluorescent probe for the detection of Al^{3+}, Bi^{3+}, Co^{2+}, Cu^{2+}, Fe^{3+}, and Cd^{2+}. The detection mechanisms of the perovskite fluorescent sensor is mostly related to luminescence-quenching mechanisms. The introduction of metal ions in perovskite solutions will quench the PL performance of perovskite materials. However, the excellent PL properties of $MAPbBr_3$ and $CsPbBr_3$ are due to the Pb^{2+} ion. The high toxicity of Pb^{2+} is a considerable concern for the future applications of the lead halide perovskite fluorescent probe. In this work, we report on the use of MABr solution for the selective and sensitive detection of Pb^{2+}. The MABr solution detects the Pb^{2+} due to the luminescence enhancing effect which is different from the quenching mechanisms of lead halide perovskite fluorescent probes.

Experimental Section

All materials were purchased from Xi'an Polymer Light Technology Corp (China). The MABr solution was prepared by dissolving 0.8 mmol MABr in 1 ml N, N-dimethylformamide (DMF). To detect the Pb^{2+} concentration, different amounts of $PbBr_2$, PbI_2 and $PbCl_2$ powders were added into MABr solutions to form the MABr@$PbBr_2$, MABr@$PbI_2$and MABr@$PbCl_2$ precursor solutions, respectively. After stirring the precursor solutions at room temperature for 30 min, the MABr@$PbBr_2$, MABr@PbI_2 and MABr@$PbCl_2$ solutions were transformed into MABr@$MAPbBr_3$, MABr@$MAPbBr_{3-x}I_x$ and MABr@$MAPbBr_{3-x}Cl_x$solutions that are transparent liquids under room light. The photoluminescence (PL) emission spectra of the MABr@$MAPbBr_3$, MABr@$MAPbBr_{3-x}I_x$

[1]Institute of Applied Micro-Nano Materials, School of Science, Beijing Jiaotong University, Beijing, 100044, People's Republic of China. [2]College of Materials Science and Engineering, Beijing University of Technology, Beijing, 100124, P.R. China. *email: ylchen@bjtu.edu.cn; yzzhang@bjut.edu.cn

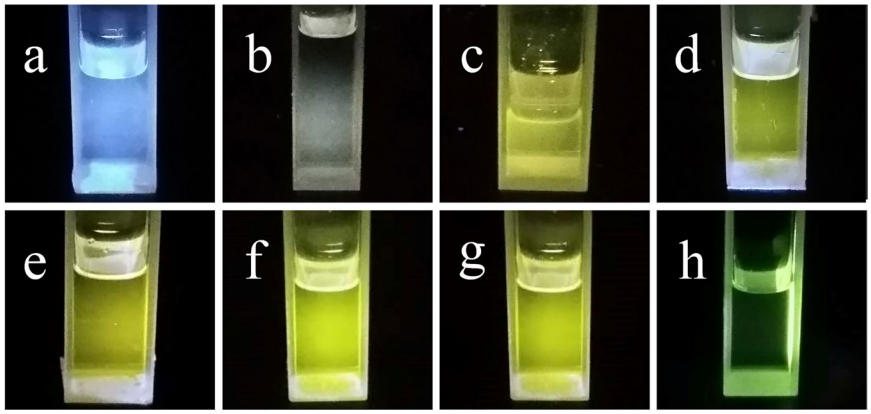

Figure 1. Photographs of $MABr@MAPbBr_3$ solutions under illumination by a 365 nm UV lamp; Pb^{2+} concentration: (**a**) 0 M (**b**) 1.6×10^{-3} M (**c**) 3.1×10^{-3} M (**d**) 6.2×10^{-3} M (**e**) 2.5×10^{-2} M (**f**) 5×10^{-2} M (**g**) 1×10^{-1} M (**h**) 2×10^{-1} M.

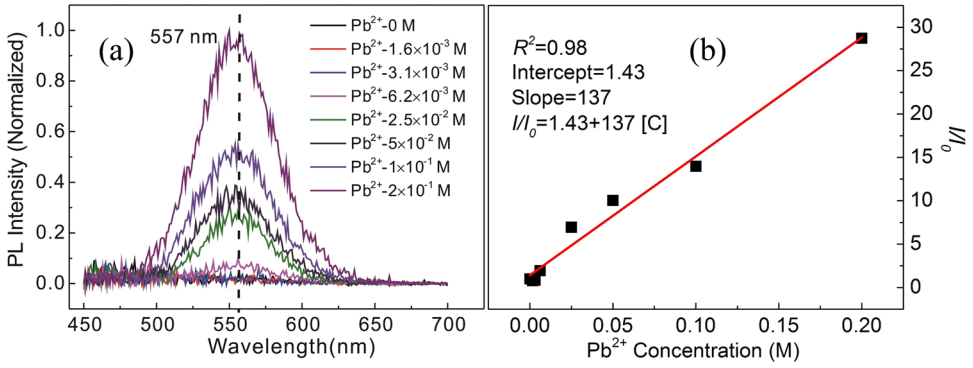

Figure 2. (**a**) PL emission spectra of $MABr@MAPbBr_3$ solutions for different Pb^{2+} concentrations for an excitation wavelength of 400 nm. (**b**) Fitting curve for the PL intensity of the $MABr@MAPbBr_3$ solutions as a function of Pb^{2+} concentration.

and $MABr@MAPbBr_{3-x}Cl_x$ solutions were measured by a photoluminescence system in the reflection mode. The time-resolved PL spectra of $MABr@MAPbBr_3$ solution were measured by an FLS980 time-resolved fluorescence spectrometer (Edinburgh Instrument). To analyze the structures of these solutions, $MABr@MAPbBr_3$ solutions were dropped on the glass substrate and then heated at 100 °C for 30 min in order to evaporate the DMF solvents. After the heat treatment, the precipitates of $MABr@MAPbBr_3$ solutions were formed on the substrate. For all of the samples on the substrates, X-ray diffraction (XRD) and scanning electron microscopy (SEM) measurements were carried out to analyze the crystal structure and morphology of the precipitate, respectively. Dynamic light scattering measurement (DLS) was conducted to analyze the size distributions of the particles in MABr and $MABr@MAPbBr_3$ solutions.

Results and Discussion

Figure 1 shows the photographs of $MABr@MAPbBr_3$ solutions under 365 nm UV lamp in a darkroom. As shown in Fig. 1(a–h), the solutions consisted of 0.8 M MABr and different amounts of $PbBr_2$ ($0–2 \times 10^{-1}$ M). All of the solutions were transparent under ambient light. The MABr solution without $PbBr_2$ only reflects the purple color of the UV light under the UV lamp illumination, as shown in Fig. 1(a), indicating that the MABr solution is nonfluorescent under the UV lamp illumination. Introduction of a small amount of $PbBr_2$ to the MABr solution leads to the formation of the $MABr@MAPbBr_3$ solution, and the $MABr@MAPbBr_3$ solution emits very pale yellow color under UV light illumination. As the Pb^{2+} concentration of the $MABr@MAPbBr_3$ solutions increased from 1.6×10^{-3} to 2×10^{-1} M, the emission colors of these solutions changed quickly from pale yellow to bright green, as shown in Fig. 1(b–h). The dependence of the photoluminescence (PL) of the $MABr@MAPbBr_3$ solutions on Pb^{2+} concentration is displayed in Fig. 2(a). All of the solutions were measured at room temperature with an excitation wavelength of 400 nm. The MABr solution does not show any florescence signal and the $MABr@MAPbBr_3$ solutions exhibit a green emission peak centered at 557 nm. However, the green emission peaks of the solutions display a large full-width-at-half-maximum (FWFM). For the $MABr@MAPbBr_3$ solution with 2×10^{-1} M Pb^{2+}, the FWFM of emission peak is 60 nm, which is larger than that of the $MABrPb_3$ thin film and powder[26–30]. Hence, a yellow green color emission is observed from the $MABr@MAPbBr_3$ solutions under the 365 nm UV lamp illumination in a darkroom (Fig. 1). The PL intensity of the MABr solution was significantly

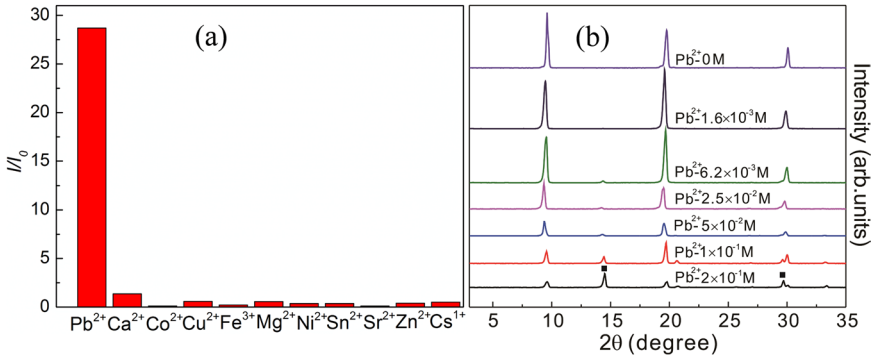

Figure 3. (**a**) PL response of the MABr solution (0.8 M) to different metal ions. (**b**) X-ray diffraction patterns of MABr@MAPbBr$_3$ solutions with different Pb^{2+} concentrations.

increased by the addition of Pb^{2+} ion in a concentration-dependent manner (Pb^{2+} concentration ranging from 0 to 2×10^{-1} M). The influence of MABr concentration on the sensitivity of Pb^{2+} detection was studied (Fig. S1). If the Pb^{2+} concentration is greater than 1×10^{-1} M, then for the same Pb^{2+} concentration, the PL intensity of the 0.8 M MABr solution is nearly the same as that of the 0.4 M MABr solution (Fig. S1). However, upon a further decrease in the Pb^{2+} concentration, the PL intensity of the 0.4 M MABr solution is much smaller that of the 0.8 M MABr solution. Hence, increasing the concentration of MABr will enhance the sensitivity for detection of Pb^{2+} ions. However, if the MABr concentration is larger than 0.8 M, the MABr powder is insoluble in the DMF solution at room temperature. Therefore, we choose the 0.8 M MABr solution as the fluorescent probe for the detection of Pb^{2+} ions.

To clarify the general applicability of MABr for Pb^{2+} detection, we replace the $PbBr_2$ powders with PbI_2 and $PbCl_2$ powders to form the MABr@PbI_2 and MABr@$PbCl_2$ precursor solutions, respectively. Figure S2 shows the PL emission spectra of MABr@PbI_2 and MABr@$PbCl_2$ solutions for different Pb^{2+} concentrations. Compared with MABr solutions, both MABr@PbI_2 and MABr@$PbCl_2$ solutions display a green emission peak under UV light illumination. For MABr@PbI_2 or MABr@$PbCl_2$ solutions, with I^- or Cl^- concentrations increase, the center of the PL emission peak gradually changed. Based on the PL measurement of MABr, MABr@$PbBr_2$, MABr@PbI_2 and MABr@$PbCl_2$ solutions, we can get the conclusion that MABr solutions exhibit luminescent response to Pb^{2+} ions. To obtain the quantitative relationship, we plotted the PL intensity of the solutions as a function of Pb^{2+} concentration (Fig. 2(b)). The relationship can be described by the following equation:

$$I/I_0 = A + K[\mathrm{C}]$$

where I and I_0 are the PL intensities of the solution in the presence and absence of Pb^{2+} ions, respectively. A and K (1/M) are the intercept and sensitivity (slope), respectively, and [C] (M) represents the Pb^{2+} concentration. The $I/I_0 - Pb^{2+}$ concentration curve can be fitted to $I/I_0 \pm \Delta(I/I_0) = 1.43 \pm 0.59 + (137.00 \pm 7.22)$ [C], with the correlation coefficient R^2 of 0.98, as shown in Fig. 2(b). The $\Delta(I/I_0)$, 0.59 and 7.22 are the standard error of I/I_0, A and K respectively. It was reported that perovskite fluorescent materials for the selective detection of metal ions or 2, 4, 6-trinitrophenol (TNP) are based on the quenching mechanism and the Stern-Volmer relationship[31]. However, the PL emission intensity of the MABr solution was enhanced with the addition of Pb^{2+}, which is different from the quenching mechanism. To evaluate the selective detection ability of the MABr solution for Pb^{2+} ions, the PL response of the MABr solution to different metal ions was explored, as shown in Fig. 3(a). The PL intensity (I) of the MABr solutions (0.8 M) after the addition of different metal ions in the same concentration (2×10^{-1} M), including Pb^{2+}, Ga^{2+}, Co^{2+}, Cu^{2+}, Fe^{3+}, Mg^{2+}, Ni^{2+}, Sn^{2+}, Sr^{2+}, and Zn^{2+}, Cs^{1+} were measured. Analysis of the PL intensity ratios I/I_0 (I_0 is the PL intensity of the MABr solution without the metal ions) of the MABr solutions with different ions showed that only Pb^{2+} gave rise to a clear PL effect for the MABr solutions, while other cations exhibit almost no PL behavior for an excitation wavelength of 400 nm or under illumination by a 365 nm UV lamp.

In order to get a better insight into the role of MABr on selective fluorescence detection of Pb^{2+} ions, the effect of interference by other metal ions were studied. Some equimolar mixtures of $PbBr_2$ (0.1 M) along with XBr (X = different metal ions) were added to the MABr solutions. The PL response of the MABr solution to equimolar mixtures of Pb^{2+} with different metal ions is shown in Fig. S3. For transparent solutions (Pb^{2+}@Ca^{2+}, Pb^{2+}@Mg^{2+}, Pb^{2+}@Sn^{2+}, Pb^{2+}@Sr^{2+}, Pb^{2+}@Zn^{2+}, Pb^{2+}@Cs^{+}), the presence of interfering ions has little impact on the luminescent response of the MABr solution to Pb^{2+}. For semitransparent solutions Pb^{2+}@Co^{2+} and Pb^{2+}@Ni^{2+}, their PL intensities are greatly lower than that of MABr@$PbBr_2$ solutions. However, compared with MABr, the MABr@$PbBr_2$@$CoBr_2$ and MABr@$PbBr_2$@$NiBr_2$ solutions still exhibit a green PL emission peak. The MABr@$PbBr_2$@$CoBr_2$ solution emits green color under UV light illumination as shown in Fig. S4. Hence, the MABr can be used to selectively detect the Pb^{2+} in the presence of Ca^{2+}, Mg^{2+}, Sn^{2+}, Sr^{2+}, Zn^{2+}, Cs^{+}, Co^{2+}, Ni^{2+}. For opaque solutions Pb^{2+}@Cu^{2+} and Pb^{2+}@Fe^{3+}, the MABr@$PbBr_2$@$CuBr_2$ and MABr@$PbBr_2$@$FeBr_3$ solutions do not show any florescence signal. Researchers also reported that Cu^{2+} leaded to dramatic quenching of the PL of perovskite materials[11,12,25]. Therefore, the MABr can't detect the Pb^{2+} in Pb^{2+}@Cu^{2+} or Pb^{2+}@Fe^{3+} solutions.

To explain the significant selective luminescent response of MABr solutions to Pb^{2+}, the structure of MABr@MAPbBr$_3$ solutions with different Pb^{2+} concentrations should be elucidated. For all of the solutions, the DMF

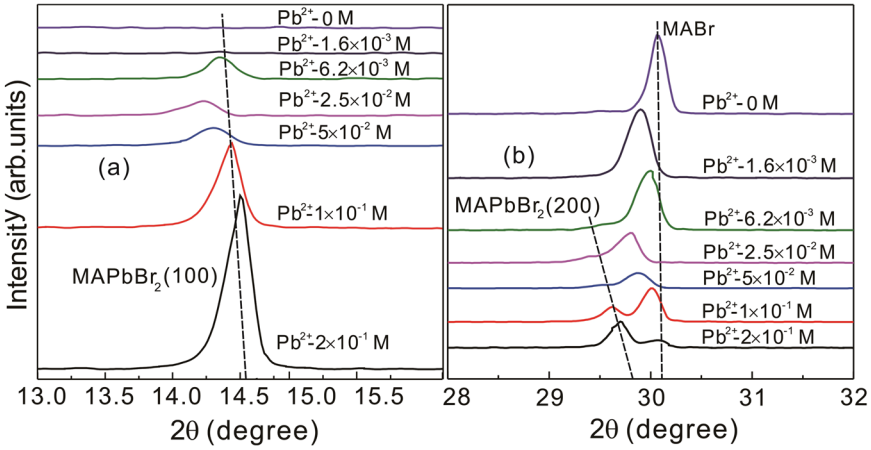

Figure 4. XRD peaks of $MAPbBr_3$ in $MABr@MAPbBr_3$ solutions with different Pb^{2+} concentrations (**a**) (100) and (**b**) (200) peak.

solvents were evaporated on the glass substrates, and then we obtained $MABr@MAPbBr_3$ films that were analyzed by XRD. Figure 3(b) shows the XRD patterns of these films with different Pb^{2+} concentrations from top to bottom at room temperature. The XRD patterns of the MABr powder and MABr thin films were measured (Fig. S5). For the MABr solutions without $PbBr_2$ (top spectrum in Fig. 3(b)), all of the diffraction peaks are the characteristic peaks of MABr. As Pb^{2+} concentration increases, the MABr peaks intensities gradually decrease and new diffraction peaks of $MAPbBr_3$ indicated by squares appear in the XRD patterns presented in Fig. 3(b). The evolution of $MAPbBr_3$ peaks with Pb^{2+} concentration is shown in Fig. 4(a,b). The XRD results (Fig. 4) show that the two peaks' intensities gradually increase with increasing Pb^{2+} concentration, corresponding to the increasing crystalline characteristics of $MAPbBr_3$ with a preferential orientation in the (100) and (200) directions. Our previous study also found that $MAPbBr_3$ thin films prepared with high MABr concentration exhibit partial preferential orientation along the (100) and (200) directions[28,29]. The (100) and (200) peaks shift toward larger angles with increasing Pb^{2+} concentration, indicating that the lattice constant of $MAPbBr_3$ is decreasing. Due to the preferential orientation, we calculated the lattice parameters of $MAPbBr_3$ from the (100) and (200) diffraction peaks. For the film with 2×10^{-1} M Pb^{2+}, the lattice constant of $MAPbBr_3$ is 6.10 Å which is larger than the previously reported value[28,29]. However, our research indicated that when Pb^{2+} concentration increased to 1×10^{-1} M, the lattice constant of $MAPbBr_3$ was 5.93 Å which is closer to the values reported by other researchers[26,27]. To further confirm the $MAPbBr_3$ phase in $MABr@MAPbBr_3$ films, we studied the morphology of these films with SEM measurements.

Figure 5 shows the morphologies of the films prepared with $MABr@MAPbBr_3$ solutions with different Pb^{2+} concentrations. An examination of Fig. 5(a,b) shows that the surface exhibits two different nonuniform aggregation morphologies. The first type of aggregation shows a shapeless morphology which is characteristic of the MABr organic compound. The other kind of aggregation is composed of cubic-shaped crystals, which is the crystalline morphology of $MAPbBr_3$. The SEM results are consistent with the XRD analyses that indicate that this film is composed of MABr and $MAPbBr_3$ phases as shown in Figs 3(b) and 4. When the $PbBr_2$ concentration in the precursor solution is reduced, the number of $MAPbBr_3$ crystals formed in the films decreased, as shown in Fig. 5(c,d). For the solution with 1.6×10^{-3} M Pb^{2+}, the morphology of the film displays highly dense MABr aggregation with high coverage and only a small amount of $MAPbBr_3$ crystals are observed on top of the MABr as shown in Fig. 5(e,f). We did not find any phases other than MABr and $MAPbBr_3$ in the XRD patterns and SEM images of the films prepared by evaporating the DMF solvents from the $MABr@MAPbBr_3$ solutions. To further exploring the interactions between MABr and $PbBr_2$, the size distributions of the particles formed in MABr and $MABr@MAPbBr_3$ solutions were measured by Dynamic Light Scattering (DLS), as shown in Fig. S6. The high MABr concentration (0.8 M) tends to form a gel-like solution and its hydrodynamic particle diameter is 650.1 nm, indicating the formation of MA^+ organic aggregates. Adding $PbBr_2$ in MABr solution increases the particles size. With Pb^{2+} concentration increased to 0.2 M, the diameter of the particles in $MABr@MAPbBr_3$ solutions increased from 650.1 to 783.5 nm. The added $PbBr_2$ might quickly react with Br^- and MA^+ to generate $PbBr_6$ octahedron inorganic frame and then self-assemble into $MAPbBr_3$ perovskite lattice. Adding $PbBr_2$ in MABr solutions would provide more nucleating sites and growth spaces, resulting in the formation of bigger aggregates in $MABr@MAPbBr_3$ solutions. Hence, addition of a small amount of $PbBr_2$ to a high MABr concentration solution and stirring of this mixture could lead to a rapid chemical reaction to form $MAPbBr_3$.

The significant luminescent response of the MABr solution to Pb^{2+} arises from the outstanding photoluminescence properties of $MAPbBr_3$. The detection limit is an important indicator of the fluorescence detector performance. As the $PbBr_2$ concentration was reduced to 1.6×10^{-3} M, the PL emission peak and diffraction peaks associated with the $MAPbB_3$ can no longer be observed in the PL emission spectra (Fig. 2) and XRD patterns (Figs 3(b) and 4), respectively. When the $PbBr_2$ concentration is lower than 1.6×10^{-3} M, only the diffraction peak of MABr could be clearly observed in the XRD pattern. However, the MABr solution with 1.6×10^{-3} M $PbBr_2$ shows a pale yellow color under UV light illumination and we can still find the $MAPbBr_3$ crystals in SEM images,

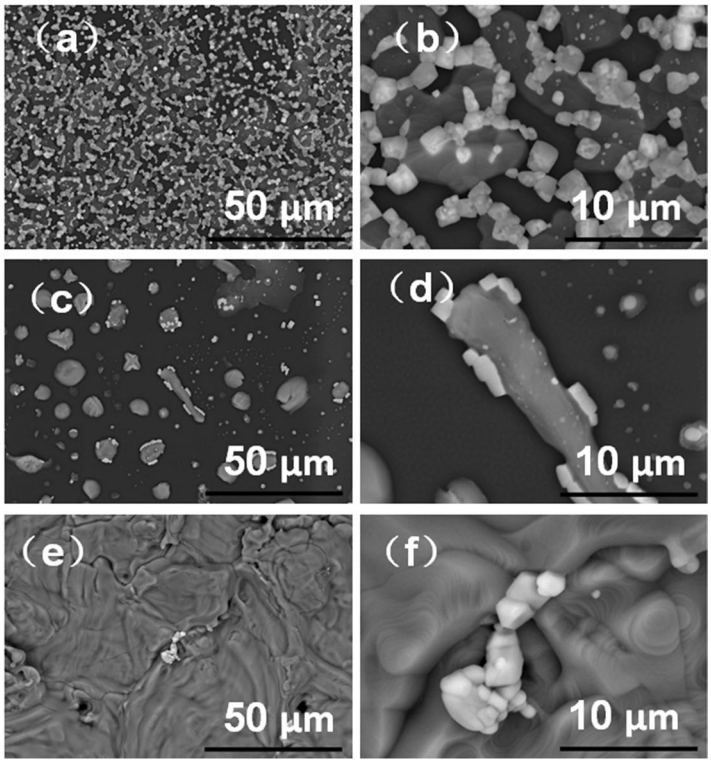

Figure 5. Low-magnification and high-magnification SEM images of the MABr@$MAPbBr_3$ solutions with different Pb^{2+} concentrations; Pb^{2+}— 2×10^{-1} M (**a,b**), Pb^{2+}— 5×10^{-2} M (**c,d**), Pb^{2+}— 1.6×10^{-3} M (**e,f**).

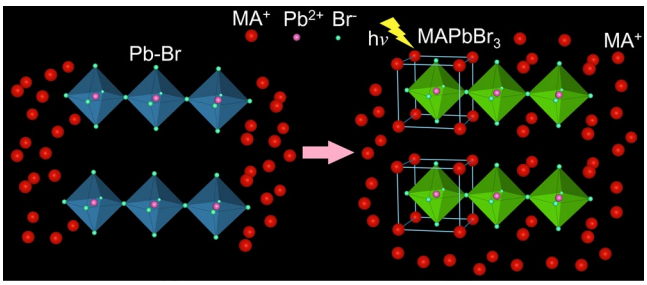

Figure 6. Schematic representation for the luminescent response of the MABr solution to Pb^{2+}.

unlike for the MABr solution without $PbBr_2$. Therefore, the detection limit of the 0.8 M MABr solution for Pb^{2+} is at least as low as 1.6×10^{-3} M. Compared with other methods[7–10] whose detection limits for Pb^{2+} are μM, the sensitivity of the MABr is not high. However, the MABr fluorescent sensor also displays many advantages such as low cost, rapid detection and ease of use. For the MABr fluorescent sensor, to selectively detect the Pb^{2+} from other metal ions, we only need a UV lamp equipment which is very cheap and easy to use. Moreover, the high MABr concentration solutions can quickly react with Pb^{2+} to form $MAPbBr_3$, which can be used to extract Pb^{2+} from liquid waste in recycling applications. Other heavy metal detectors can't extract Pb^{2+} from liquid waste. We also justify the luminescent response of MABr to Pb^{2+} on paper strips, as shown in Fig. S7. The letters "BJTU" were written with $PbBr_2$ solution (0.1 M) on paper strips. The "BJTU" are invisible on paper strips under ambient light. However, after loading of MABr solutions (0.8 M) on these paper strips, the "BJTU" show bright green emission pattern under UV light illumination.

Based on these results, the fluorescence sensing mechanism can be schematically represented as shown in Fig. 6. To obtain excellent performance in a photovoltaic device, it is necessary to lower the rate of the chemical reaction between MABr and $PbBr_2$ to form uniform $MAPbBr_3$ films with good surface coverage[32–34]. However, for fluorescence sensors or detectors with a short response time, we seek to make MABr react with $PbBr_2$ to form $MAPbBr_3$ as quickly as possible. Excess MABr contributes to speeding up the transformation from $PbBr_2$ to $MAPbBr_3$. On the other hand, a MABr-rich environment gives rise to MABr residue that encompasses the $MAPbBr_3$ crystal after the reaction. Thus, the use of excess MABr leads to the formation of a high amount of defects. The recombination lifetimes of the MABr@$MAPbBr_3$ solution with 2×10^{-1} M Pb^{2+} is only 1.33 ns (Fig. S8). For perovskite materials, the recombination lifetime is related to crystallite dimension, the larger

crystallites (e.g. single crystal) present longer photoluminescence lifetime. However, in our research, the DLS and SEM studies indicate that the MABr@$MAPbBr_3$ solutions display big aggregates (783.5 nm) which consist of organic aggregates and $MAPbBr_3$ crystals. Because of the organic aggregates and numerous defects, the MABr@$MAPbBr_3$ solutions display a short-lived PL lifetime. In fact, the spin-coating method could evaporate some of the used MABr. We used a MABr@$MAPbBr_3$ solution with 2×10^{-1} M Pb^{2+} as the precursor solution and spin-coated it on the glass substrate to obtain the MABr@$MAPbBr_3$ thin film. The SEM images exhibit that the number of MABr residues of the MABr@$MAPbBr_3$ thin film prepared by the spin-coating method is smaller than that of the MABr@$MAPbBr_3$ film prepared by evaporating the DMF solutions (Figs 5(a,b) and S9). For $MAPbBr_3$ films, a previous study also indicated that the introduction of Cl was conducive to the evaporation of the excess MABr during the spin-coating process[32–34]. If the MABr in MABr@$MAPbBr_3$ solutions can be removed completely, we can obtain $MAPbBr_3$ material with excellent photovoltaic performance. Therefore, the MABr solution not only can be used to detect the Pb^{2+} heavy metal but also may extract the Pb^{2+} from the liquid waste for reuse.

Conclusion

In summary, our research indicates that MABr can be used as a new platform for selective fluorescence detection of Pb^{2+} ions. The incorporation of $PbBr_2$ into a MABr solution formed $MAPbBr_3$@MABr solutions that exhibit significant luminescent responses under UV light illumination. The significant color changes of the MABr solutions before and after the addition of $PbBr_2$ under UV lamp illumination can be observed by the naked eye. The PL intensity of the MABr sensor increases with increasing Pb^{2+} concentration, exhibiting a linear relationship. The fluorescence sensing mechanism of MABr for Pb^{2+} is due to the excellent PL performance of $MAPbBr_3$ in $MAPbBr_3$@MABr solutions. Some MABr in $MAPbBr_3$@MABr solutions can be evaporated by the spin-coating method, enabling the extraction of Pb^{2+} from the liquid waste for recycling use. These findings may contribute to the development of new applications for luminescent perovskite materials.

Data availability

The datasets analysed during the current study are available from the corresponding author on reasonable request.

Received: 10 April 2019; Accepted: 17 October 2019;
Published online: 01 November 2019

References

1. Winneke, G., Brockhaus, A., Ewers, U., Kramer, U. & Neuf, M. Results from the European multicenter study on lead neurotoxicity in children: implications for risk assessment. *Neurotoxicol. Teratol.* **12**, 553–559 (1990).
2. Wang, S. & Mulligan, C. N. Occurrence of arsenic contamination in Canada: sources, behavior and distribution. *Sci. Total Environ.* **366**, 701–721 (2006).
3. Sorg, T. J., Chen, A. S. C. & Wang, L. Arsenic species in drinking water wells in the USA with high arsenic concentrations. *Water Res.* **48**, 156–169 (2014).
4. Xing, W., Zhao, Q., Scheckel, K. G., Zheng, L. & Li, L. Inhalation bioaccessibility of Cd, Cu, Pb and Zn and speciation of Pb in particulate matter fractions from areas with different pollution characteristics in Henan Province, China. *Ecotoxicol. Environ. Saf.* **175**, 192–200 (2019).
5. Ding, Y. *et al*. Binding characteristics of heavy metals to humic acid before and after fractionation by ferrihydrite. *Chemosphere* **226**, 140–148 (2019).
6. Jin, M. *et al*. Synergistic effects of Pb and repeated heat pulse on developmental neurotoxicity in zebrafish. *Ecotoxicol. Environ. Saf.* **172**, 460–470 (2019).
7. Shkinev, V. M., Gomolitskii, V. N. & Spivakov, B. Y. Determination of trace heavy metals in waters by atomic-absorption spectrometry after preconcentration by liquid-phase polymer-based retention. *Talanta* **36**, 861–863 (1989).
8. Sondergaard, J., Asmund, G. & Larsen, M. M. Trace Elements Determination in Seawater by ICP-MS With On-line Preconcentration on a Chelex-100 Column Using a 'standard' Instrument Setup. *MethodsX* **2**, 323–330 (2015).
9. Tonguc, O. T., Yilmaz, S., Turkoglu, M. & Dilgin, Y. Determination of heavy metal pollution with environmental physicochemical parameters in waste water of Kocabas Stream (Biga, Canakkale, Turkey) by ICP-AES. *Environ. Monit. Assess.* **127**, 389–397 (2006).
10. Dutta, S., Strack, G. & Kurup, P. Gold nanostar electrodes for heavy metal detection. *Sens. Actuators, B* **281**, 383–391 (2019).
11. Sarkar, S., Chatti, M. & Mahalingam, V. Highly Luminescent Colloidal Eu^{3+}-Doped $KZnF_3$ Nanoparticles for the Selective and Sensitive Detection of Cu-II Ions. *Chem. Eur. J.* **20**, 3311–3316 (2014).
12. Zhang, D. W., Xu, Y., Liu, Q. L. & Xia, Z. G. Encapsulation of $CH_3NH_3PbBr_3$ Perovskite Quantum Dots in MOF-5 Microcrystals as a Stable Platform for Temperature and Aqueous Heavy Metal Ion Detection. *Inorg. Chem.* **57**, 4613–4619 (2018).
13. Wang, Q. L., Tao, L. M., Jiang, X. X., Wang, M. K. & Shen, Y. Graphene oxide wrapped $CH_3NH_3PbBr_3$ perovskite quantum dots hybrid for photoelectrochemical CO_2 reduction in organic solvents. *Appl. Surf. Sci.* **465**, 607–613 (2019).
14. Wang, K. H., Li, L. C., Shellaiah, M. & Sun, K. W. Structural and Photophysical Properties of Methylammonium Lead Tribromide ($MAPbBr_3$) Single Crystals. *Sci. Rep.* **7**, 13643 (2017).
15. Luo, Y. *et al*. Direct Observation of Halide Migration and its Effect on the Photoluminescence of Methylammonium Lead Bromide Perovskite Single Crystals. *Adv. Mater.* **29**, 1703451 (2017).
16. Ji, X. *et al*. On the performance of polymer:organometal halide perovskite composite light emitting devices: The effects of polymer additives. *Org. Electron.* **52**, 350–355 (2018).
17. Tang, X. *et al*. Ultrathin, Core–Shell Structured SiO2 Coated Mn^{2+}-Doped Perovskite Quantum Dots for Bright White Light-Emitting Diodes. *Small* 1900484 (2019).
18. Yang, D. *et al*. Surface Halogen Compensation for Robust Performance Enhancements of $CsPbX_3$ Perovskite Quantum Dots. *Adv. Optical Mater*. 1900276 (2019).
19. Zhang, X. *et al*. Strong Blue Emission from Sb^{3+}-Doped Super Small $CsPbBr_3$ Nanocrystals. *J. Phys. Chem. Lett.* **10**, 1750–1756 (2019).
20. Park, M. H. *et al*. Efficient Perovskite Light-Emitting Diodes Using Polycrystalline Core Shell-Mimicked Nanograins. *Adv. Funct. Mater*. 1902017 (2019).
21. Wang, Q., Ren, J., Peng, X. F., Ji, X. X. & Yang, X. H. Efficient Sky-Blue Perovskite Light-Emitting Devices Based on Ethylammonium Bromide Induced Layered Perovskites. *ACS Appl. Mater. Interfaces* **9**, 29901–29906 (2017).
22. Lin, K. *et al*. Perovskite light-emitting diodes with external quantum efficiency exceeding 20 per cent. *Nature* **562**, 245–248 (2018).
23. Zhang, C. *et al*. Conversion of invisible metal-organic frameworks to luminescent perovskite nanocrystals for confidential information encryption and decryption. *Nat. Commun.* **8**, 1138 (2017).

24. Muthu, C., Nagamma, S. R. & Nair, V. C. Luminescent hybrid perovskite nanoparticles as a new platform for selective detection of 2, 4, 6-trinitrophenol. *RSC Adv.* **4**, 55908–55911 (2014).
25. Liu, Y. *et al*. All–inorganic $CsPbBr_3$ perovskite quantum dots as photoluminescent probe for ultrasensitive Cu^{2+} detection. *J. Mater. Chem. C.* **6**, 4793–4799 (2018).
26. Zhang, M. *et al*. Composition-dependent photoluminescence intensity and prolonged recombination lifetime of perovskite $CH_3NH_3PbBr_{3-x}Cl_x$ films. *Chem. Commun.* **50**, 11727–11730 (2014).
27. Baikie, T. *et al*. A combined single crystal neutron/X-ray diffraction and solid-state nuclear magnetic resonance study of the hybrid perovskites $CH_3NH_3PbX_3$ (X = I, Br and Cl). *J. Mater. Chem. A* **3**, 9298–9307 (2015).
28. Yan, J., Ke, X. H., Chen, Y. L., Zhang, A. & Zhang, B. Effect of modulating the molar ratio of organic to inorganic content on morphology, optical absorption and photoluminescence of perovskite $CH_3NH_3PbBr_3$ films. *Appl. Surf. Sci.* **351**, 1191–1196 (2015).
29. Yan, J., Zhang, B., Chen, Y. L., Zhang, A. & Ke, X. H. Improving the Photoluminescence Properties of Perovskite $CH_3NH_3PbBr_{3-x}Cl_x$ Films by Modulating Organic Cation and Chlorine Concentrations. *ACS Appl. Mater. Interfaces.* **8**, 12756–12763 (2016).
30. Zhang, B., Yan, J., Wang, J. & Chen, Y. L. Effect of the modulating of organic content on optical properties of single-crystal perovskite. *Opt. Mater.* **62**, 273–278 (2016).
31. Boaz, H. & Rollefson, G. K. The Quenching of Fluorescence Deviations from the Stern-Volmer Law. *J. Am. Chem. Soc.* **72**, 3435–3443 (1950).
32. Yu, H. *et al*. The role of chlorine in the formation process of "$CH_3NH_3PbI_{3-x}Cl_x$" perovskite. *Adv. Funct. Mater.* **24**, 7102–7108 (2014).
33. Edri, E., Kirmayer, S., Kulbak, M., Hodes, G. & Cahen, D. Chloride Inclusion and Hole Transport Material Doping to Improve Methyl Ammonium Lead Bromide Perovskite-Based High Open-Circuit Voltage Solar Cells. *J. Phys. Chem. Lett.* **5**, 429–433 (2014).
34. Chen, Q. *et al*. The optoelectronic role of chlorine in $CH_3NH_3PbI_3$ (Cl)-based perovskite solar cells. *Nat. Commun.* **6**, 7269 (2015).

Acknowledgements

This work is financially supported by National Natural Science Foundation of China (Nos 51802014, 61875235) and the Fundamental Research Funds for the Central Universities (No. 2019JBM068).

Author contributions

J.Y., Y.C. and Y.Z. designed the experiments. J.Y. and Y.H. carried out all the experiments. H.Y. advised on the overall experiments with critical comments. J.Y. wrote the manuscript and all authors have given approval to the final version of the manuscript.

Competing interests

The authors declare no competing interests.

Additional information

Supplementary information is available for this paper at https://doi.org/10.1038/s41598-019-52431-y.

Correspondence and requests for materials should be addressed to Y.C. or Y.Z.

Reprints and permissions information is available at www.nature.com/reprints.

Publisher's note Springer Nature remains neutral with regard to jurisdictional claims in published maps and institutional affiliations.

Open Access This article is licensed under a Creative Commons Attribution 4.0 International License, which permits use, sharing, adaptation, distribution and reproduction in any medium or format, as long as you give appropriate credit to the original author(s) and the source, provide a link to the Creative Commons license, and indicate if changes were made. The images or other third party material in this article are included in the article's Creative Commons license, unless indicated otherwise in a credit line to the material. If material is not included in the article's Creative Commons license and your intended use is not permitted by statutory regulation or exceeds the permitted use, you will need to obtain permission directly from the copyright holder. To view a copy of this license, visit http://creativecommons.org/licenses/by/4.0/.

© The Author(s) 2019